

# End-to-end Triple-domain PET Enhancement: A Hybrid Denoising-and-reconstruction Framework for Reconstructing Standard-dose PET Images from Low-dose PET Sinograms

Caiwen Jiang<sup>a</sup>, Mianxin Liu<sup>d</sup>, Kaicong Sun<sup>a</sup> and Dinggang Shen<sup>a,b,c,\*</sup>

<sup>a</sup>School of Biomedical Engineering & State Key Laboratory of Advanced Medical Materials and Devices, ShanghaiTech University, Shanghai, China

<sup>b</sup>Shanghai United Imaging Intelligence Co., Ltd., Shanghai, China

<sup>c</sup>Shanghai Clinical Research and Trial Center, Shanghai, 201210, China

<sup>d</sup>Shanghai Artificial Intelligence Laboratory, Shanghai 200232, China

## ARTICLE INFO

### Keywords:

Positron emission tomography (PET)  
Hybrid denoising-and-reconstruction  
LPET-to-SPET reconstruction  
Triple-domain  
Transformer  
Discrete wavelet transform

## ABSTRACT

As a sensitive functional imaging technique, positron emission tomography (PET) plays a critical role in early disease diagnosis. However, obtaining a high-quality PET image requires injecting a sufficient dose (standard dose) of radionuclides into the body, which inevitably poses radiation hazards to patients. To mitigate radiation hazards, the reconstruction of standard-dose PET (SPET) from low-dose PET (LPET) is desired. According to imaging theory, PET reconstruction process involves multiple domains (e.g., projection domain and image domain), and a significant portion of the difference between SPET and LPET arises from variations in the noise levels introduced during the sampling of raw data as sinograms. In light of these two facts, we propose an end-to-end Triple-domain LPET Enhancement (TriPLET) framework, by leveraging the advantages of a hybrid denoising-and-reconstruction process and a triple-domain representation (i.e., sinograms, frequency spectrum maps, and images) to reconstruct SPET images from LPET sinograms. Specifically, TriPLET consists of three sequentially coupled components including 1) a Transformer-assisted denoising network that denoises the inputted LPET sinograms in the projection domain, 2) a discrete-wavelet-transform-based reconstruction network that further reconstructs SPET from LPET in the wavelet domain, and 3) a pair-based adversarial network that evaluates the reconstructed SPET images in the image domain. Extensive experiments on the real PET dataset demonstrate that our proposed TriPLET can reconstruct SPET images with the highest similarity and signal-to-noise ratio to real data, compared with state-of-the-art methods.

## 1. Introduction

Positron emission tomography (PET) is a non-invasive and sensitive imaging technique with an essential role in early disease diagnosis and intervention in clinics (Xiang, Wang, Gong, Zaharchuk and Zhang, 2020; Chen, 2007b; Luo, Wang, Zu, Zhan, Wu, Zhou, Shen and Zhou, 2021; Sakthivel, Thakar, Prashanth, Angamuthu, Sharma and Kumar, 2020). By injecting the radionuclides into the body and capturing the emitted positron signals, PET can visualize the metabolic and biochemical processes in the body by assessing the radionuclides' distributions (Maurer and Wang, 2005; Decazes, Hinault, Veresezan, Thureau, Gouel and Vera, 2021). This characteristic makes PET a valuable imaging modality for precise diagnoses of diseases, particularly for diseases such as cancer and Alzheimer's disease (Jiang, Pan, Cui and Shen, 2022; Dimitrakopoulou-Strauss, Pan and Sachpekidis, 2021).

But the radionuclides used in PET imaging are radioactive, which inevitably poses a risk of radiation exposure to patients (Buchbender, Heusner, Lauenstein, Bockisch and Antoch, 2012). In addition, due to limitations in signal receiver sensitivity and noise interference, the dose of radionuclides must meet a certain threshold to produce

PET images with sufficient quality for clinical diagnosis (Amirrahedi, Sarkar, Ghadiri, Ghafarian and Ay, 2021; Kreisl, Kim, Coughlin, Henter, Owen and Innis, 2020). Despite applying the As Low As Reasonably Achievable (ALARA) (Slovic and Thomas, 2002) principle in clinical imaging to minimize radiation exposure, PET imaging may still be deemed unacceptable for certain populations, such as pediatric subjects and pregnant women (Lei, Dong, Wang, Higgins and Yang, 2020; Barbosa, Queiroz, Nunes, Costa, Zaniboni, Marin, Cerri and Buchpiguel, 2020). To mitigate the radiation risks associated with PET imaging, designing advanced reconstruction algorithms to enhance PET image quality (e.g., reconstructing standard-dose PET (SPET) from low-dose PET (LPET)) is a promising alternative.

In recent decades, many PET enhancement methods have been developed, with most of those methods focusing only on SPET reconstruction in a single domain, typically the image domain. However, it is important to note that during the reconstruction process, PET data are not limited to images alone but can be represented in multiple forms, each emphasizing different aspects of information. For instance, PET data can be represented as sinograms, images, and frequency spectrum maps in the projection, image, and wavelet domains, respectively, as depicted in Figure 1. These domains can be converted to each other in a lossless fashion using the Radon transform (Hamil, Michel and Kinahan, 2003) and discrete wavelet transform (WT) (Bhavana and

\*Corresponding author.

✉ dgshen@shanghaitech.edu.cn (Dinggang Shen)

ORCID(s):

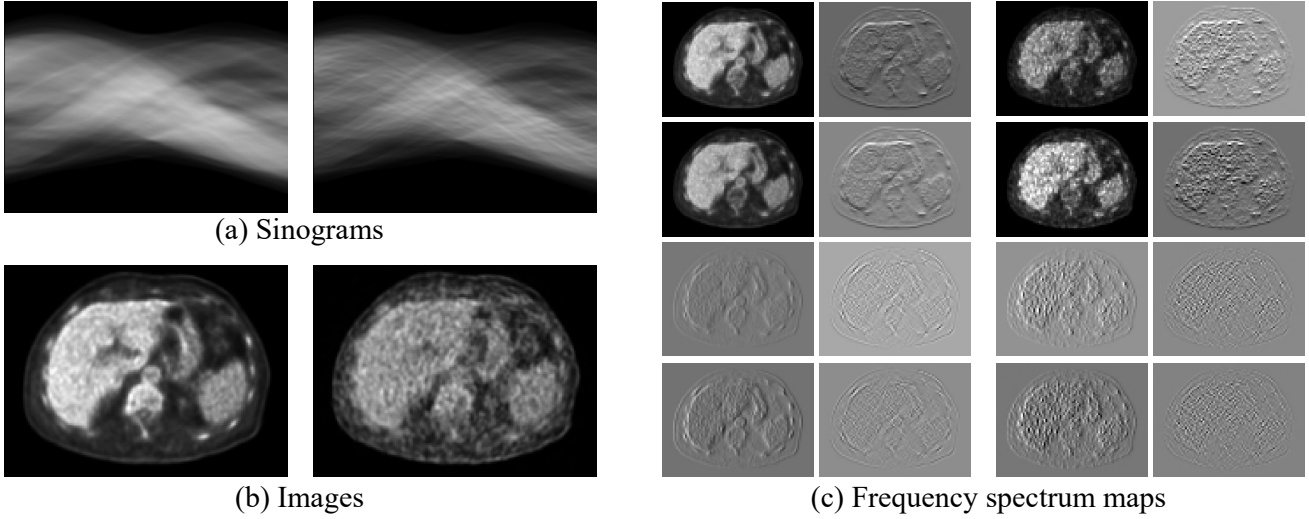


**Figure 1:** Representation of PET data in three domains: (a) projection domain, (b) image domain, and (c) wavelet domain, with the SPET and LPET shown on the left and right of each subfigure, respectively. Radon transform and discrete wavelet transform can convert PET data between images and sinograms, and also between images and frequency spectrum maps, respectively. After applying discrete wavelet transform, a 3D PET image can be decomposed into eight frequency spectrum maps of different sub-bands.

Krishnappa, 2015). Therefore, the incorporation of multiple domains in the design of reconstruction algorithms is expected to lead to significant improvements.

In addition, another important fact is that PET data is initially sampled as a sinogram and then subsequently reconstructed into an image (Fahey, 2002). Furthermore, a significant distinction between LPET and SPET lies in the discrepancy in noise levels within the sinogram (Mokri, Saripan, R., Nordin, Hashim and Marhaban, 2016). Thus, it is useful to adopt a hybrid denoising-and-reconstruction framework for incorporating a sinogram noise reduction step before reconstruction. This approach can align more closely with the actual reconstruction process and effectively suppress the propagation and amplification of noises inherent in the raw data (sinogram) during the subsequent processing.

Accordingly, we propose an end-to-end TriPLE-domain LPET EnhancemT (TriPLET) framework, by considering a hybrid denoising-and-reconstruction process and simultaneously taking the advantages of projection, wavelet, and image domains in reconstructing SPET from LPET. The TriPLET is based on our previous work TriDoRNet (Jiang, Pan and Shen, 2023) and comprises 1) a denoising network to initially remove noises from the inputted LPET sinograms in the projection domain, 2) a reconstruction network to refine the denoising process and also reconstruct SPET from LPET in the wavelet domain, and 3) an adversarial network to evaluate the reconstructed SPET images in the image domain. The most significant differences between TriPLET and TriDoRNet include 1) The denoising network architecture has been redesigned, i.e., in the current work, the denoising network adopts an alternating structure of CNN and transformer blocks to achieve improved denoising effects. 2) An adversarial network has been integrated into the framework, and a paired adversarial loss has been designed to make

the reconstructed SPET images more closely resemble real images. 3) The GradNorm (Chen, Badrinarayanan, Lee and Rabinovich, 2018) technique has been used to automatically adjust the weights of different loss functions during training, reducing the difficulty of tuning parameters. 4) Due to the use of different methodologies, the related research background, literature review, and experimental design have also been different from our previous work.

Among these networks, the denoising network adopts a residual learning strategy to predict the residual sinogram, and further integrates Transformer modules to capture noises as long-range representations contained in the sinogram. The reconstruction network follows the 3D U-Net architecture, but replaces both downsampling and upsampling operations with wavelet transform (WT) and inverse wavelet transform (IWT), respectively, to allow the network to work on the wavelet frequency domains for preserving high-frequency structural details. The adversarial network takes two pairs of images, i.e., the predicted SPET & LPET images and the real SPET & LPET images, as the inputs, to properly discriminate the fake image pair from the real image pair for facilitating accurate reconstruction. Furthermore, to improve the supervision in training the TriPLET, we design an integrated loss function by combining constraints in the projection, wavelet, and image domains.

The main contributions of this work can be summarized as follows:

1. To leverage the advantages of projection, wavelet, and image domains in reconstructing SPET from LPET, we propose an end-to-end TriPLE-domain LPET EnhancemT (TriPLET) framework coupled by a denoising network, a reconstruction network, and an adversarial network.

2. To facilitate the reconstruction, we adopt a hybrid denoising-and-reconstruction framework by incorporating a sinogram noise reduction step before reconstruction. This framework allows an end-to-end reconstruction in the practical sampling process. Additionally, we design a transformer-based denoising network to capture the long-range information in the LPET sinogram.
3. To enhance the structural details of the reconstructed SPET images, we incorporate discrete wavelet transform into the reconstruction network, which enables the network to capture important frequency band information of PET.
4. Extensive experiments conducted on clinical chest-abdomen PET data show superior performance of our approach over state-of-the-art methods in SPET image reconstruction.

The subsequent sections of this paper are structured as follows. Section II provides an overview of the related work, while Section III presents a detailed description of our proposed approach. Implementation details and experimental results are presented in Section IV. Finally, our work is summarized in Section V.

## 2. Related Work

In this section, we provide a comprehensive review of related works in two specific domains, including PET enhancement and multi-domain image reconstruction, to better illustrate our SPET enhancement task and our motivation for leveraging multi-domain representation into the reconstruction process.

### 2.1. PET Enhancement

In recent years, many enhancement algorithms have been developed to improve PET image quality. The first set of methods are the filtering-based methods that are used to remove noise from LPET images. Typical methods include the non-local mean (NLM) filter with or without anatomical information (Buades, Coll and Morel, 2005; Chan, Meikle, Fulton, Tian, Cai and Feng, 2009), block-matching 3D (BM3D) filtering and its higher dimensional variants BM4D and BM5D (Dabov, Foi, Katkovnik and Egiazarian, 2006; Ote, Hashimoto, Kakimoto, Isobe, Inubushi, Ota, Tokui, Saito, Moriya and Omura, 2020), wavelet filter (for removing noise from specific frequency sub-bands) (P., Hanzouli, Hatt, R. and Visvikis, 2013), and guided filter (by integrating cross-modality information) (Yan, Lim and Townsend, 2015). These methods are quite robust, but tend to over-smooth images and suppress high-frequency details.

The second set of methods is the machine learning-based algorithms. For instance, Kang *et al.* (Kang, Gao, Shi, Lalush, Lin and Shen, 2015) introduced a random forest-based approach to predict SPET images at the voxel level. Wang *et al.* (Wang, Zhang, An, Ma, Kang, Shi, Wu, Zhou, Lalush and Lin, 2015) proposed a mapping-based sparse learning method that leverages LPET images and

corresponding MR images for SPET image prediction. An *et al.* (An, Zhang, Adeli, Wang, Ma, Shi, Lalush, Lin and Shen, 2016) developed a data-driven multi-level correlation analysis methodology that utilizes LPET and MRI images for SPET image generation. However, due to the unavailability of corresponding MR images for most PET images, Wang *et al.* (Wang, Ma, An, Shi, Zhang, Wu, Zhou and Shen, 2016) proposed a semi-supervised triple dictionary learning method that incorporates a large number of unpaired training samples in the SPET image generation process. Nonetheless, these methods often require manual intervention and are time-consuming, which hinders their widespread application in clinic.

Currently, deep learning-based methods, leveraging the advantages of convolutional neural networks (CNNs) in image processing (Kleesiek, Urban, Hubert, Schwarz, Maier-Hein, Bendszus and Biller, 2016; Kawahara, Brown, Miller, Booth and Hamarneh, 2017), have emerged as the dominant approach for PET enhancement. Several mapping networks, such as 3D CNN (Kim, Wu, Gong, Dutta, Kim, Son, Kim, F. and Li, 2018), conditional GAN (Wang, Yu, Wang, Zu, Lalush, Lin, Wu, Zhou, Shen and Zhou, 2018), locally adaptive GAN (Wang, Zhou, Yu, Wang, Zu, Lalush, Lin, Wu, Zhou and Shen, 2019), and adaptive rectification GAN (Luo, Zhou, Zhan, Fei, Zhou, Wang and Shen, 2022), have been proposed to generate SPET images from LPET images. However, a common drawback of these methods is their reliance on paired LPET and SPET images for supervision. To overcome this limitation, unsupervised methods based on deep image prior and Noise2Noise have been introduced. For instance, Cui *et al.* (Cui, Gong, Guo, Wu, Meng, Kim, Zheng, Wu, Fu, Xu *et al.*, 2019) proposed an unsupervised deep learning-based method for PET denoising, which utilizes a prior high-quality image from the patient as the network input and the noisy PET image itself as the training label. Onishi *et al.* (Onishi, Hashimoto, Ote, Ohba, Ota, Yoshikawa and Ouchi, 2021) developed an unsupervised PET image denoising method that incorporates an anatomical information-guided attention mechanism, leveraging anatomical information from MR to guide PET denoising. However, these unsupervised methods require alternative-modality images, such as MR/CT, to serve as guiding images, and the predicted PET images often retain some residual content from MR/CT due to the lack of explicit supervision. Additionally, some studies have explored the direct reconstruction of SPET images from LPET sinograms. For example, Häggström *et al.* (Häggström, Schmidtlein, Campanella and Fuchs, 2019) proposed a deep learning model, called DeepPET, which reconstructs PET images directly from sinogram data without relying on system and noise models. Feng *et al.* (Feng and Liu, 2020) introduced a PET reconstruction framework that employs two coupled networks to directly reconstruct high-quality PET images from ultra-low-dose sinograms. These deep learning-based methods are significantly different from time-consuming traditional PET reconstruction algorithms, such as Ordered Subset Expectation Maximization (OSEM) (Byrd, Dasari,



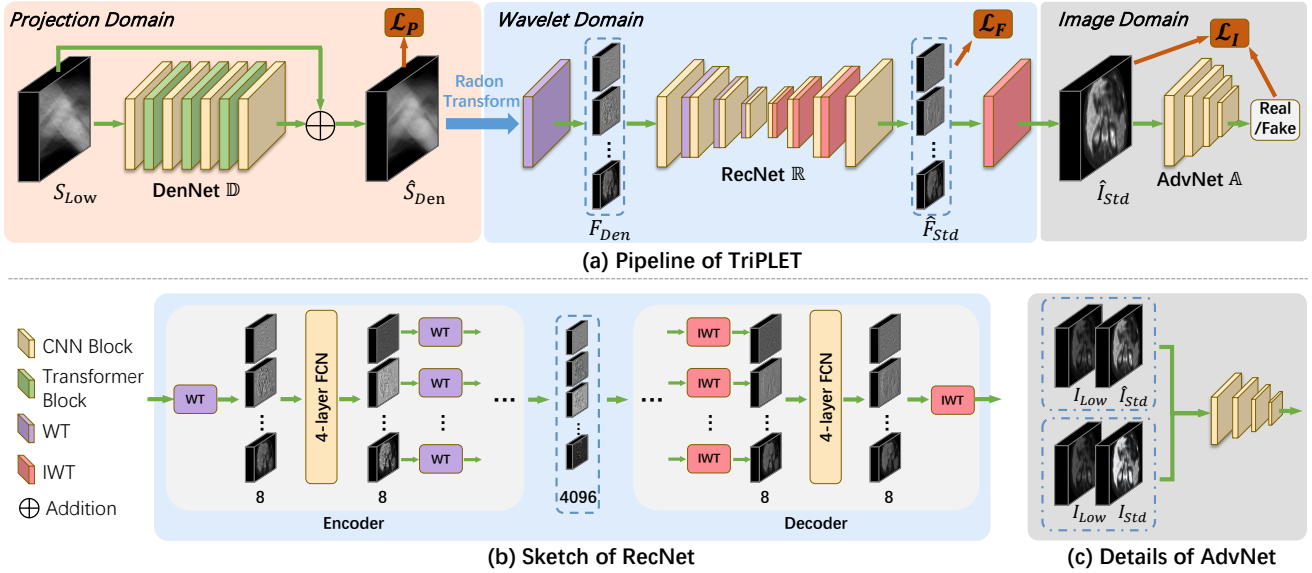


**Figure 2:** Our proposed TriPLET involves three domains, i.e., the projection, wavelet, and image domains. PET data have different representations in each domain, such as the LPET sinogram  $S_{Low}$  and the denoised sinogram  $S_{Den}$  in the projection domain, the denoised frequency spectrum map  $F_{Den}$  and the predicted SPET map  $\hat{F}_{Std}$  in the wavelet domain, and the LPET image  $I_{Low}$ , the predicted SPET image  $\hat{I}_{Std}$ , and the actual SPET image  $I_{Std}$  in the image domain. We have also designed specific loss functions  $\mathcal{L}_P$ ,  $\mathcal{L}_F$ , and  $\mathcal{L}_I$  to supervise the prediction results in each domain.

Jansen and Kinahan, 2023), since, in the application stage, the reconstructed image can be obtained by going through a single forward the trained network (without iterative optimization).

## 2.2. Multi-domain Image Reconstruction

According to imaging theory, multiple domains are involved in reconstructing medical images (e.g., PET, MR, and CT) from the original signals, thus considering multiple domains in designing reconstruction algorithms may achieve successful improvement. This has been demonstrated in various studies. For instance, Arabi *et al.* (Arabi and Zaidi, 2018) introduced a hybrid dual-domain PET denoising method that combines advantages of both image and projection domains to preserve image textures while minimizing quantification uncertainty. Souza *et al.* (Souza, Lebel and Frayne, 2019) proposed a hybrid frequency-/image-domain cascade of convolutional neural networks (CNNs) with intercalated data consistency layers for MR image reconstruction. Wu *et al.* (Wu, Hu, Niu, Yu, Vardhanabhuti and Wang, 2021) developed a dual-domain residual-based optimization network for CT image reconstruction, sequentially operating in the projection and image domains. Zhou *et al.* (Zhou, Chen, Zhou, Duncan and Liu, 2022) presented a dual-domain data consistent recurrent network that reconstructs artifact-free images through recurrent image domain and projection domain restorations. The successes of these previous works have served as inspiration for our design of the end-to-end triple-domain PET enhancement (TriPLET) framework.

## 2.3. Adversarial Learning in Medical Image

Adversarial learning (Goodfellow, Pouget-Abadie, Mirza, Xu, Warde-Farley, Ozair, Courville and Bengio, 2014) is

an essential technique in the deep learning field. It involves training by placing a generative model and a discriminative model in an adversarial framework, where the generative model aims to generate data as close to real data as possible, and the discriminative model tries to distinguish between real and generated data. This setup forces both generative and discriminative models to continuously improve during the training process, thereby enhancing the quality of the generated data. Due to this advantage, adversarial learning strategies have been widely adopted in many medical image analysis studies (Yi, Walia and Babyn, 2019). For example, Hu *et al.* (Hu, Yu, Chen and Wang, 2020) develop a data augmentation method based on generative adversarial networks to reconstruct missing PET images from MRI for AD assessment. Sun *et al.* (Sun, Wang, Huang, Ding, Greenspan and Paisley, 2020) propose a medical image synthesis model named abnormal-to-normal translation generative adversarial network (ANT-GAN) to generate a normal-looking medical image based on its abnormal-looking counterpart without the need for paired training data. Li *et al.* (Li, Zhang, Shi, Miao and Jiang, 2021) introduce a medical image denoising method based on conditional Generative Adversarial Networks (cGAN) for medical image denoising tasks.

## 3. Method

Figure 2 (a) illustrates the pipeline of our TriPLET. When given an LPET sinogram  $S_{Low}$ , TriPLET first applies the denoising network (DenNet)  $\mathbb{D}$  to denoise it in the projection domain. Next, the reconstruction network (RecNet)  $\mathbb{R}$  reconstructs the SPET image  $I_{Std}$  from the denoised sinogram  $S_{Den}$  in the wavelet domain. Finally, the adversarial

network (AdvNet)  $\mathbb{A}$  evaluates the predicted SPET image  $\hat{I}_{Std}$  in the image domain. Moreover, we design respective loss functions, including  $\mathcal{L}_P$ ,  $\mathcal{L}_F$ , and  $\mathcal{L}_I$ , to supervise the prediction results of each network. Subsequently, we introduce the construction of sub-networks and the design details of each loss function.

### 3.1. Denoising Network

Compared to SPET, LPET exhibits stronger noise during imaging due to its weaker signal strength, which is directly reflected in the raw data of PET, i.e., the sinogram. To effectively prevent the propagation and amplification of noise during the subsequent processing and also align our enhancement framework more closely with the actual PET reconstruction process, we incorporate a noise reduction procedure for sinogram before reconstruction. Hence, we design a denoising network (DenNet)  $\mathbb{D}$  in the projection domain to denoise the LPET sinogram  $S_{Low}$ . As shown in Figure 2 (a),  $\mathbb{D}$  uses the residual learning strategy to predict residual sinograms with seven blocks, where the  $\{1^{st}, 3^{rd}, 5^{th}, 7^{th}\}$  and  $\{2^{nd}, 4^{th}, 6^{th}\}$  blocks are the CNN blocks and Transformer blocks, respectively. Its uniqueness lies in the *Residual Learning Strategy* and *Capturing Long-range Information via Transformer*, as described below. (Song, Yang and Dutta, 2021)

*Residual Learning Strategy:* We design the denoising network  $\mathbb{D}$  based on the concept of residual learning (Zhang, Zuo, Chen, Meng and Zhang, 2017), which is commonly utilized in various denoising tasks. Specifically,  $\mathbb{D}$  is designed to predict the residual sinogram which represents the difference between denoised sinogram  $S_{Den}$  and SPET sinogram  $S_{Std}$  rather than directly predicting the  $S_{Den}$ . In this way, we can estimate noisy components (the residual parts) and effectively avoid gradient vanishing while also enhancing the network's ability to learn the underlying features of the sinogram by enabling it to have a larger number of layers.

*Capturing Long-range Information via Transformer:* According to projection theory, the signals collected in PET imaging are represented as the line of response (LOR) in the sinogram. This means that noise is also represented as LOR in the sinogram with non-local (long-range) representation. The limited perceptual field in the conventional convolutional neural network makes it hard to capture such long-range information. Therefore, we incorporate CNNs with the Transformer (Liu, Lin, Cao, Hu, Wei, Zhang, Lin and Guo, 2021) blocks into the denoising network to address this issue. Compared to CNN, the Transformer is better at capturing long-range information, making it more suitable for the sinogram with long-range representation but at the cost of higher computational demands. Considering the balance between performance and computational cost, our denoising network employs a hybrid structure of CNN and Transformer blocks. Moreover, alternately using CNN and Transformer blocks allows for the effective extraction of local information by CNN blocks and global information by Transformer blocks, which has been successful in some studies (Geng, Tan, Wang, Jia, Zhang and Yan, 2024; Yang,

He and Zhang, 2023). Inspired by the success of these works, our denoising network ultimately adopts an alternating combination of 3 CNN blocks and 3 Transformer blocks.

For the CNN blocks, we employ a Conv+BN+ReLU architecture. Specifically, Conv is the convolutional layer with a kernel size of  $3 \times 3 \times 3$  and a stride of 1, BN is the batch normalization with a batch size of 4, and ReLU stands for rectified linear units, which are used for introducing non-linearity. The features outputted by the CNN block are subsequently inputted into the Transformer block. Figure 3 illustrates the architectural details of the Transformer blocks. Each Transformer block consists of a window-based multi-head self-attention (W-MSA) module and a 2-layer multi-layer perceptron (MLP) module. To ensure stable training, layer normalization (LN) layers are inserted before each MSA and MLP module, and a residual connection is applied after each module. The input for the Transformer block is formed by treating each voxel of the feature map along the channel dimension as a sequence. The W-MSA module adopts the same windowing operation as Swin Transformer (Liu et al., 2021), i.e., computing attention in the partitioned windows, instead of the whole feature maps. Specifically, in the W-MSA module, we split the feature map evenly into non-overlapping windows with a size of  $4 \times 4 \times 4$  and compute self-attention within each local window. Meanwhile, to preserve the spatial information, we encode position information along three directions according to (Carion, Massa, Synnaeve, Usunier, Kirillov and Zagoruyko, 2020). The final position encoding is obtained by concatenating the position encodings along these three directions. By adopting a hybrid architecture (consisting of alternating CNN and Transformer blocks), we can enhance the denoising network's capacity to capture long-range information while effectively keeping computational efficiency.

### 3.2. Reconstruction Network

By applying the Radon transform to the outputs of the denoising network, we can obtain the denoised images. Then, we use the reconstruction network (RecNet)  $\mathbb{R}$  to reconstruct the SPET images  $\hat{I}_{Std}$  from the denoised images. However, due to the nature of PET imaging, which reflects metabolic and biochemical activities rather than structural details, the inherent structural information in PET images is not as prominent as in other structural imaging modalities such as CT and MR. Thus, preserving and enhancing high-frequency structural information in the LPET to SPET reconstruction process poses a challenge. To address this, we incorporate the discrete wavelet transform (WT) (Liu, Zhang, Zhang, Lin and Zuo, 2018) into the reconstruction network. By dividing the PET image into several sub-band frequency spectrum maps, we can better reconstruct information of each sub-band, resulting in the reconstructed SPET image containing richer structural details. As shown in Figure 2 (b), we utilize discrete wavelet transform (WT) and inverse wavelet transform (IWT) in the reconstruction network  $\mathbb{R}$  as a substitute for the traditional upsampling operations (such as zero-padding) and downsampling operations

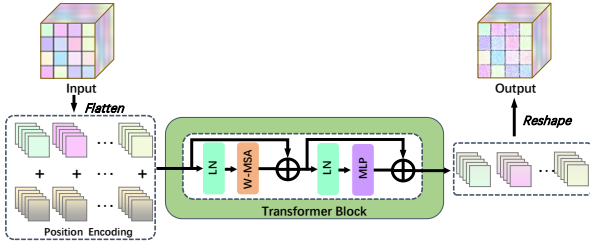


**Figure 3:** Architectural detail of the Transformer block in the DenNet (denoising network).

(such as max-pooling). Specifically,  $\mathbb{R}$  includes an encoder and a decoder. First, the denoised image is passed through the encoder to generate 4096 sub-band frequency spectrum maps. Then, these frequency spectrum maps are utilized as the input of the decoder to reconstruct the SPET image  $\hat{I}_{Std}$ .

In the encoder, WT, instead of the pooling operation, is used to reduce the size of feature maps. Passing through a WT operation, an image/feature map is decomposed into eight sub-band feature maps of reduced size (e.g., a  $256 \times 256 \times 160$  image will be decomposed into eight  $128 \times 128 \times 80$  sub-band feature maps). We totally cascade four WT operations in the encoder, each followed by a fully CNN block consisting of four  $3 \times 3 \times 3$  convolutional layers (each with batch normalization (BN) and rectified linear unit (ReLU) operations). After passing through the encoder, the input denoised image will be decomposed into 4096 feature maps. Considering that the relationship among different sub-bands may be useful to the reconstruction, we regard the sub-band feature maps as a concatenation along the channel dimension, rather than independent feature maps, when feeding into the CNN blocks.

In the decoder, correspondingly, four inverse wavelet transforms (IWTs) are cascaded for upsampling. Contrary to WT, IWT composes eight sub-band feature maps into one feature map/image of larger size (e.g., composing eight  $128 \times 128 \times 80$  sub-band feature maps into one  $256 \times 256 \times 160$  feature map). Each IWT is followed by a CNN block, similar to WT in the encoder. The only difference is that the last layer of the last CNN block has no BN and ReLU, which is adopted to predict the final result. That is, through the decoder, the 4096 sub-band feature maps produced by the encoder will be finally composed into one image ( $\hat{I}_{Std}$ ).

### 3.3. Adversarial Network

In clinical practice, PET data is typically utilized in the image domain for diagnosis purposes, where information is obtained from images instead of sinograms or feature maps. As such, the main objective of our TriPLET is to produce high-quality SPET representations in the image domain, even if it involves multiple representations of PET data. To achieve this, we designed the adversarial networks (AdvNet)  $\mathbb{A}$  in the image domain to evaluate the quality of the  $\hat{I}_{Std}$  output from the reconstruction network.

As shown in Figure 2 (c),  $\mathbb{A}$  takes two image pairs as input, including the fake pair and the real pair. The fake pair

consists of the LPET image  $I_{Low}$  and the predicted SPET image  $\hat{I}_{Std}$ , while the real pair contains the LPET image  $I_{Low}$  and the actual SPET image  $I_{Std}$ . When being fed into the network, the images in each pair are concatenated along the channel dimension. The purpose of including LPET in the input of  $\mathbb{A}$  is to impose an additional condition constraint on the discriminative process. In this way, we can reduce the difficulty of discrimination while ensuring the generator ( $\mathbb{D}$  and  $\mathbb{R}$ ) to produce a correct SPET image (corresponding to the structure of the inputted LPET, instead of an arbitrary SPET that just matches the real SPET distribution). The architecture of  $\mathbb{A}$  is based on the traditional discriminator (Isola, Zhu, Zhou and Efros, 2017). Specifically, it comprises four convolutional layers, with the first three using Leaky-ReLU activation functions and the last one using a sigmoid activation function to classify the input image pair as either real or fake.

### 3.4. Loss Function

While training our TriPLET, constraints in the projection, frequency, and images domains are all adopted, which are denoted as  $\mathcal{L}_P$ ,  $\mathcal{L}_F$ , and  $\mathcal{L}_I$ , respectively. Using  $\mathcal{L}_P$ ,  $\mathcal{L}_F$ , and  $\mathcal{L}_I$  to supervise the training of TriPLET has two main benefits. On the one hand, our TriPLET consists of three sub-networks (i.e., denoising, reconstruction, and adversarial networks), and  $\mathcal{L}_P$ ,  $\mathcal{L}_F$ , and  $\mathcal{L}_I$  are designed specifically for these three sub-networks. Utilizing  $\mathcal{L}_P$ ,  $\mathcal{L}_F$ , and  $\mathcal{L}_I$  allows for better training of these sub-networks, thereby reducing the overall training difficulty of TriPLET. On the other hand, as mentioned in (Abouhawwash and Alessio, 2022), multiple learning objectives can enhance the overall quality of the reconstructed images from various perspectives, resulting in high-quality images that better meet the needs of practical applications. Specifically,  $\mathcal{L}_P$  is performed in the projection domain, which is the mean square error (MSE) of the output of  $\mathbb{D}$  against the SPET sinogram  $S_{Std}$ . The calculation of MSE is given by Equation 5. Hence, we can define  $\mathcal{L}_P$  as below:

$$\mathcal{L}_P = \mathcal{L}_{MSE}(S_{Std}, \mathbb{D}(S_{Low})). \quad (1)$$

$\mathcal{L}_F$  is performed in the wavelet domain to impose constraints on all eight frequency spectrum maps that are output from the  $\mathbb{R}$ . Specifically,  $\mathcal{L}_F$  utilize the focal frequency loss (FFL) (Jiang, Dai, Wu and Loy, 2021), which assigns varying weights to different elements of the frequency spectrum maps, i.e., larger weights for hard-to-reconstruct elements and smaller weights for easy-to-reconstruct elements. To achieve this,  $\mathcal{L}_F$  introduces the weight matrices  $\mathcal{W} = [w_1, w_2, \dots, w_8]$  with the same size as frequency spectrum maps that is dynamically determined by a nonuniform distribution on the current loss of each element during training. Let  $F_{Std} = [f_1, f_2, \dots, f_8]$  and  $\hat{F}_{Std} = [\hat{f}_1, \hat{f}_2, \dots, \hat{f}_8]$  be the frequency spectrum maps of actual SPET image and predicted SPET image, respectively, and then the value of the weight matrix  $w_i$  at  $(u, v, k)$  can be calculated as:

$$w_i(u, v, k) = |f_i(u, v, k) - \hat{f}_i(u, v, k)|^\alpha, \quad (2)$$

where  $\alpha$  is the scaling factor for flexibility and set to 1 in our implementation. Next, we normalize values of  $w_i$  to fall within the range  $[0,1]$  to obtain  $\bar{w}_i$ , and perform a Hadamard product between the weight matrices  $\bar{w}_i$  and the frequency distance matrices. This yields the complete form of  $\mathcal{L}_F$ :

$$\mathcal{L}_F = \sum_{i=1}^8 (\bar{w}_i \odot \mathcal{L}_{MSE}(f_i, \hat{f}_i)). \quad (3)$$

$\mathcal{L}_I$  is performed in the image domain, considering two aspects. First, we calculate the MSE between the predicted SPET image  $\hat{I}_{Std}$  and the actual SPET image  $I_{Std}$ , denoted as  $\mathcal{L}_{I\_MSE} = \mathcal{L}_{MSE}(I_{Std}, \hat{I}_{Std})$ . Additionally, we incorporate the adversarial loss generated by the adversarial network  $\mathbb{A}$ , denoted as  $\mathcal{L}_{I\_Adv}$ . The formulation of  $\mathcal{L}_{I\_Adv}$  is as follows:

$$\mathcal{L}_{I\_Adv} = (\mathbb{A}(I_{Low}, I_{Std}) - 1)^2 + \mathbb{A}(I_{Low}, \hat{I}_{Std})^2, \quad (4)$$

where  $\mathbb{A}(\cdot)$  represents the output probability of AdvNet. It serves as a measure of the likelihood or confidence assigned to a given input.

### 3.5. Training Details

We adopt a multi-stage training strategy to reduce the difficulty of training TriPLET, which divides the training process into three stages. In the first stage,  $\mathbb{D}$  is independently supervised by  $\mathcal{L}_P$ . In the second stage,  $\mathbb{D}$ ,  $\mathbb{R}$ , and  $\mathbb{A}$  are co-supervised by the combination of  $\mathcal{L}_F$  and  $\mathcal{L}_I$  (including  $\mathcal{L}_{I\_MSE}$  and  $\mathcal{L}_{I\_Adv}$ ). It should be noted that in this stage, only the parameters of  $\mathbb{R}$  and  $\mathbb{A}$  are updated, while  $\mathbb{D}$  is kept frozen. In the third stage,  $\mathbb{D}$ ,  $\mathbb{R}$ , and  $\mathbb{A}$  are co-supervised by the combination of  $\mathcal{L}_P$ ,  $\mathcal{L}_F$ , and  $\mathcal{L}_I$  and fine-tuned with a smaller learning rate. In the second and third stages, we utilize the GradNorm (Chen et al., 2018) technique to combine different loss functions, which allows for dynamic adjustment of the weights of the different losses based on their gradients during training.

The experiments are performed using the PyTorch platform and a single NVIDIA Tesla V100 GPU. Each of the three stages is trained for a total of 300 epochs using the Adam optimizer, and the learning rates for the three stages are set to 0.001, 0.001, 0.0001, respectively.

## 4. Experiments

### 4.1. Data Description

For the evaluation of TriPLET, we collect a dataset of 70 paired chest-abdomen SPET and LPET images from the uEXPLORER PET/CT scanner (Zhang, Xie, Berg, Judenhofer, Liu, Xu, Ding, Lv, Dong and Deng, 2020) whose relevant parameters are given in Table 1. Paired LPET and SPET images are acquired using the list mode of the scanner with an injection of 256 MBq of  $[^{18}\text{F}]$ -FDG injection. The SPET images are reconstructed using 1200s data between 60 minutes and 80 minutes after injection by ordered-subsets

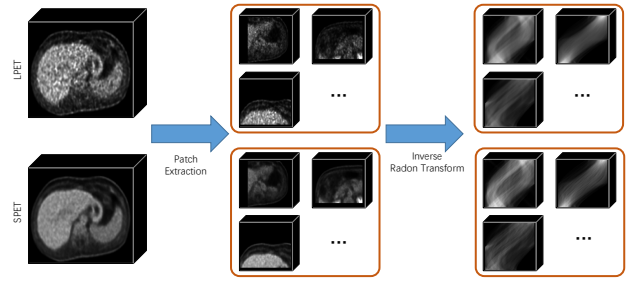


**Figure 4:** Process of extracting image patches and sinogram patches from the whole PET image.

**Table 1**

Physical characteristics of uEXPLORER scanner.

Parameter	Description
Scintillator	Lutetium-yttrium oxorthosilicate
Photodetectors	Silicon photomultiplier
Crystal pitch and depth	$2.85 \times 2.85 \times 18.1$ mm
Total number of crystals	564,480
AFOV	194 cm
Detector ring diameter	78.6 cm
Transaxial field of view	68.6 cm
TOF resolution	430 ps
Energy resolution	11.7 %
Number of lines of response	$\leq 90$ billion before accounting for TOF
Maximum axial (polar) angle	$57^\circ$

expectation maximization (OSEM) algorithm (Mehranian and Reader, 2020), while the corresponding 1/10th LPET images are simultaneously reconstructed using 120s data uniformly sampled from the 1200s data.

In the preprocessing stage, we uniformly resample all images to a voxel spacing of  $1 \times 1 \times 1$  mm<sup>3</sup> and a resolution of  $256 \times 256 \times 160$ . We filter each PET image's values (i.e., only retaining values within the 5% to 95% range) to eliminate outliers, thereby removing their influence on subsequent tasks. Then, the intensity range of the images is normalized to  $[0, 1]$  using Z-score normalization. To increase the number of training samples and reduce the dependence on GPU memory, we extract overlapping patches of size  $96 \times 96 \times 96$  from each whole PET image. As shown in Figure 4, all patch extraction operations are performed in the image domain, and the corresponding sinogram patches are converted from the extracted image patches through inverse Radon transform. The sinogram and image can be losslessly converted between each other through Radon transform and inverse Radon transform (Toft, 1996). Hence, this method of obtaining sinogram patches does not introduce additional errors and ensures consistency between image patches and sinogram patches. It should be noted that our patch extraction operation is directly applied to PET images in the image domain and cannot be directly applied to PET sinograms. However, in theory, when the input is a sinogram, we can also extract patches from the sinogram and then use the Radon transform to obtain the corresponding



**Table 2**

Performance of SPET images reconstructed using five different combinations of loss functions and network components, measured by PSNR, SSIM, and rRMSE. The symbol \* indicates the significant difference between the performance of our approach and the optimal performance among other methods, at  $p$ -value  $<0.05$  level.

Method	Network	$\mathcal{L}_P$	$\mathcal{L}_F$	$\mathcal{L}_I$	PSNR [dB]↑	SSIM ↑	rRMSE ↓
I	U-Net	–	✗	✓	23.367 ± 1.372	0.983 ± 0.012	0.792 ± 0.557
II	RecNet	–	✗	✓	23.865 ± 1.486	0.985 ± 0.009	0.468 ± 0.365
III	RecNet	–	✓	✓	24.968 ± 0.973	0.988 ± 0.007	0.413 ± 0.327
IV	DenNet + RecNet	✓	✗	✓	25.341 ± 0.845	0.990 ± 0.006	0.316 ± 0.243
V (ours)	DenNet + RecNet	✓	✓	✓	<b>25.932 ± 0.671*</b>	<b>0.992 ± 0.004</b>	<b>0.296 ± 0.213*</b>

image patches. Additionally, we did not collect PET raw data (i.e., sinograms). The sinograms indirectly obtained from reconstructed PET images may indeed differ from the real PET raw data. Nevertheless, our method can still be applied to real PET raw data, although the performance might exhibit some variation. From each subject, 40 patches covering all regions-of-interest are extracted, resulting in a total of 2800 training samples.

To ensure stable results and minimize randomness, we adopted a five-fold cross-validation. In each fold, samples from 56 subjects are used for training, while the remaining subjects are used for testing. Mean and standard deviation are calculated across the five folds to report the overall performance.

## 4.2. Evaluation Metrics

In our evaluation of TriPLET, we employ three commonly used metrics in reconstruction tasks to quantitatively assess the results, including structural similarity index (SSIM) (Wang, Bovik, Sheikh and Simoncelli, 2004), relative root mean squared error (rRMSE), and peak signal-to-noise ratio (PSNR).

Specifically, the SSIM metric is particularly useful for assessing visual image quality, as it takes image structure into account. A high SSIM value indicates good image quality, with a range of  $0 \leq \text{SSIM} \leq 1$ . An SSIM value of 1 signifies that the compared image is identical to the ground-truth image.

The rRMSE metric evaluates the level of agreement between two sets of measurements by assessing the root mean squared error relative to a reference. It quantifies the accuracy of the reconstruction, with lower rRMSE values indicating higher agreement with the ground truth,

$$\text{MSE} = \frac{1}{N} \sum_{i=1}^N (x_i - y_i)^2, \quad (5)$$

$$\text{rRMSE} = \frac{\sqrt{\text{MSE}}}{\bar{y}},$$

where  $x$  is the predicted image,  $y$  is the ground-truth image,  $N$  is the number of image voxels, and  $\bar{y}$  is the all-voxel-averaged value of the ground-truth image.

And PSNR metric measures the ratio of the maximum possible power of a signal to the power of corrupting noise, with higher PSNR values indicating better agreement between the predicted image and the ground-truth image,

$$\text{PSNR} = 20 \cdot \log_{10} \left( \frac{y_{\max}}{\sqrt{\text{MSE}}} \right). \quad (6)$$

$y_{\max}$  represents the maximum value of the ground-truth image.

We use difference maps to display the qualitative results. Difference maps are obtained by subtracting the reconstructed SPET images (i.e., the actual SPET) from the GT and then taking the absolute value. In the difference maps, larger values (i.e., darker colors) indicate a larger difference between the reconstructed SPET image and the GT, while smaller values (i.e., lighter colors) indicate a smaller difference between the reconstructed SPET image and the GT.

## 4.3. Ablation Study of Key Components

To verify the contributions of different network components and loss functions of our proposed TriPLET, we perform an ablation experiment to compare the following five methods: I) U-Net supervised by  $\mathcal{L}_I$ ; II)  $\mathbb{R}$  supervised by  $\mathcal{L}_I$ ; III) RecNet supervised by  $\mathcal{L}_F$  and  $\mathcal{L}_I$ ; IV) DenNet and RecNet supervised by  $\mathcal{L}_P$  and  $\mathcal{L}_I$ ; V) DenNet and RecNet supervised by  $\mathcal{L}_P$ ,  $\mathcal{L}_F$ , and  $\mathcal{L}_I$ . It is noteworthy that the production of  $\mathcal{L}_I$  is dependent on the adversarial networks  $\mathbb{A}$ , therefore all the methods discussed above involve  $\mathbb{A}$ . Furthermore, Methods I, II, and III aim to reconstruct SPET images from LPET images, whereas Methods IV and V reconstruct SPET images from LPET sinograms. All methods use the same experimental settings, and their quantitative and qualitative results are provided in Table 2 and Figure 5, respectively.

**Benefits of Wavelet Transform:** The convolutional and pooling layers in convolutional neural networks (CNNs) tend to smooth and downsample voxels when processing



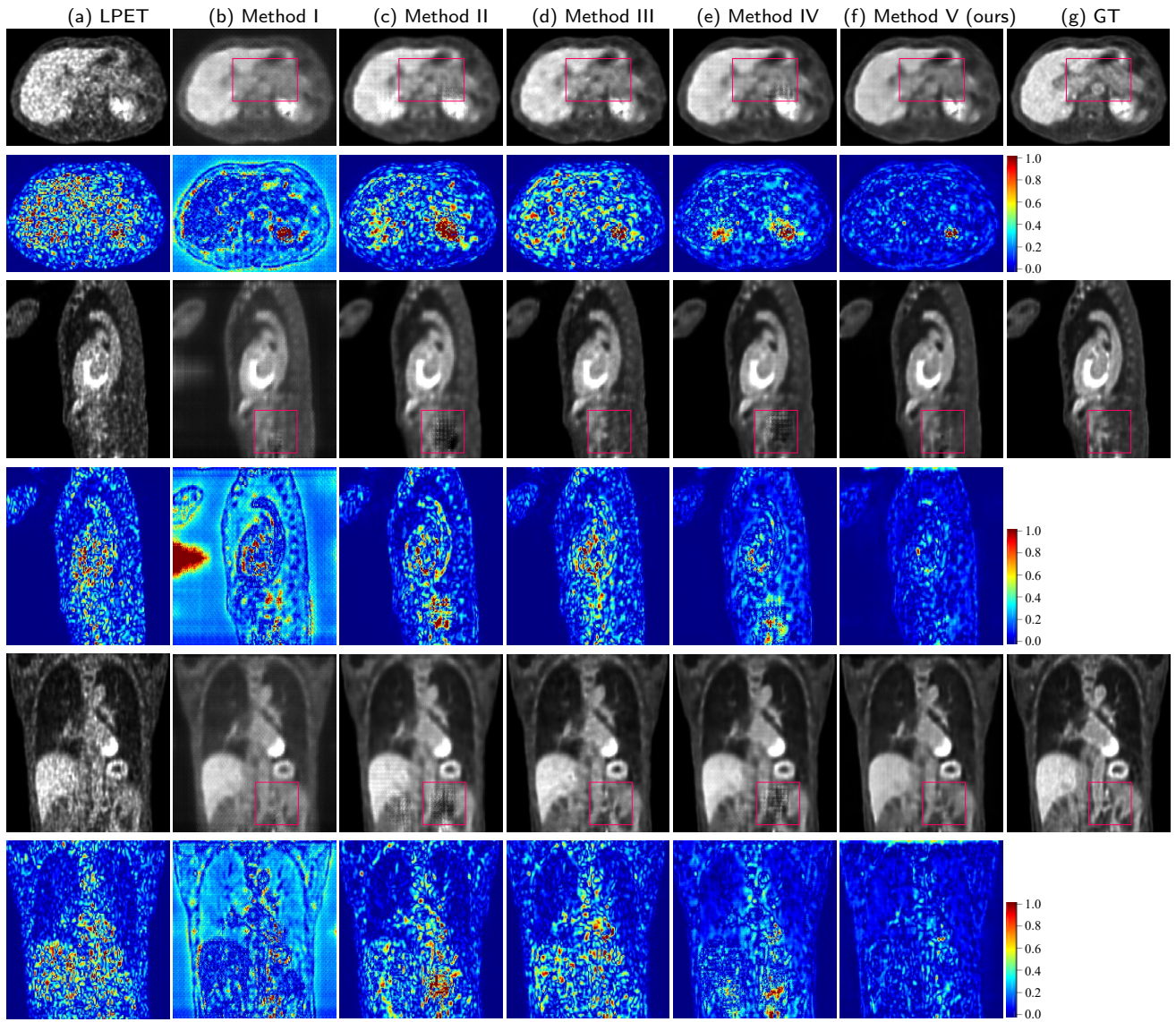


**Figure 5:** Visual comparison of SPET images produced using five different combinations of loss functions and network components shown in Table 1. The LPET image is shown on the left, followed by the results produced by the five different methods indicated in Table 1 (2nd-5th columns), and the ground truth (GT) in the last column. The corresponding difference maps between the produced results and the ground truth (GT) are depicted in the 2nd (axial view), 4th (sagittal view), and 6th (coronal view) rows. Red boxes show areas for detailed comparison.

**Table 3**

Quantitative comparison between our TriPLET and state-of-the-art SPET reconstruction methods, measured by PSNR, SSIM, and rRMSE. The symbol \* indicates the significant difference between the performance of our approach and the optimal performance among other methods, at  $p$ -value  $< 0.05$  level.

Method	PSNR [dB]↑	SSIM ↑	rRMSE ↓
cGAN	23.383 ± 1.364	0.982 ± 0.013	0.604 ± 0.483
LA-GAN	23.351 ± 1.725	0.984 ± 0.012	0.767 ± 0.551
Sinogram-Net	23.528 ± 1.634	0.986 ± 0.009	0.541 ± 0.416
Trans-GAN	23.852 ± 1.522	0.985 ± 0.011	0.452 ± 0.372
AR-GAN	25.217 ± 0.853	0.988 ± 0.007	0.377 ± 0.359
TriDoRNet	25.892 ± 0.784	0.991 ± 0.006	0.325 ± 0.286
TriPLET (ours)	<b>25.932 ± 0.671*</b>	<b>0.992 ± 0.004*</b>	<b>0.296 ± 0.213*</b>

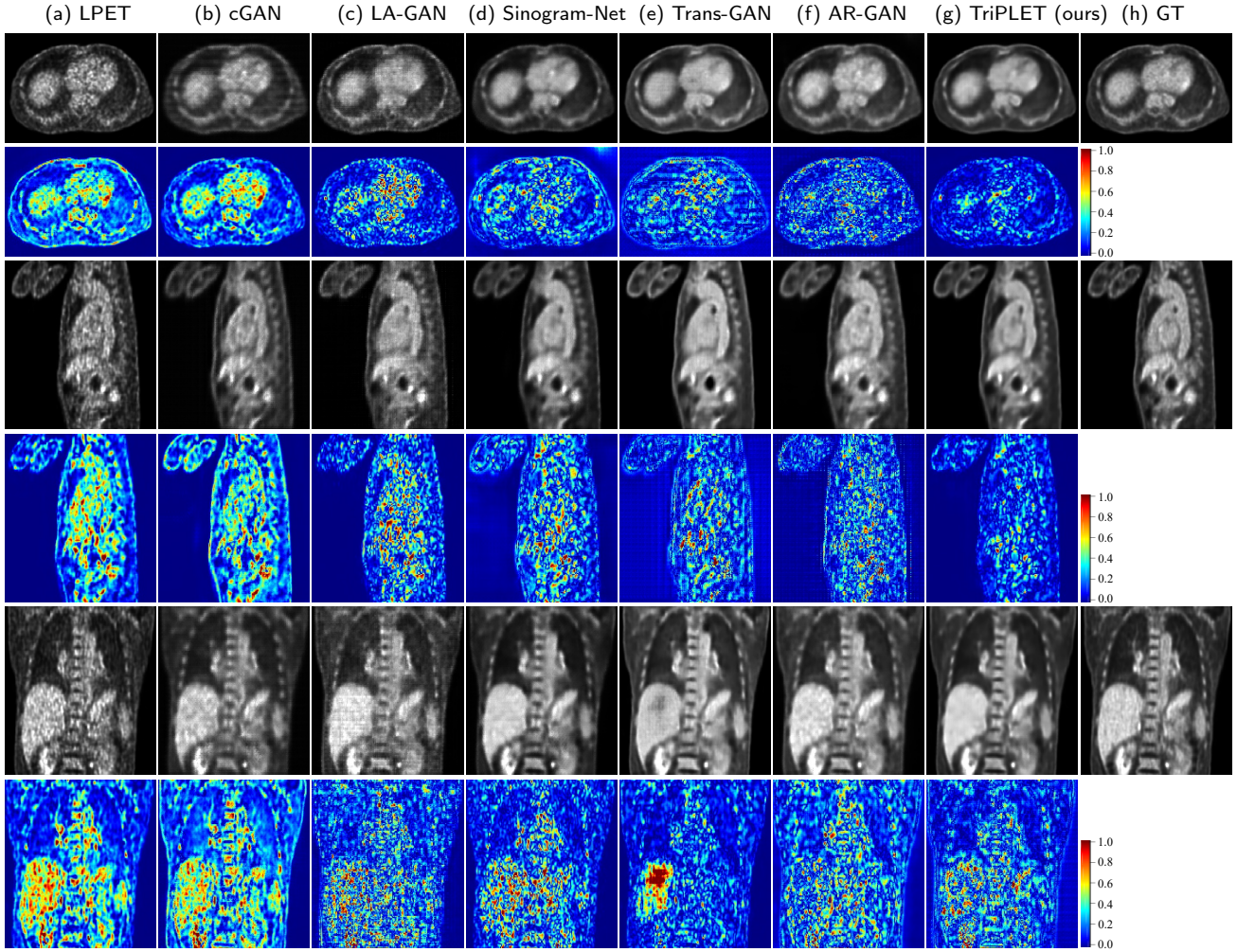


**Figure 6:** Visual comparison of SPET images generated by six different methods. The arrangement from left to right includes the LPET images, results obtained from five alternative comparison methods (2nd to 6th columns), our TriPLET (7th column), and the GT (SPET image). Additionally, the 2nd (axial view), 4th (sagittal view), and 6th (coronal view) rows display the corresponding difference maps between the generated results and the GT.

images (Huang, Guan, Chen, Zhu, Chen and Yu, 2022). This can result in detailed information loss and also the over-smoothed predicted images, which is particularly problematic for PET images that inherently lack structural details. To overcome this challenge, we incorporate discrete wavelet transform into the reconstruction network  $\mathbb{R}$  to decompose the PET images into multiple sub-band frequency spectrum maps. Our designed  $\mathbb{R}$  can decompose the high-frequency components in PET images separately through WT during reconstruction, and it is equipped with a specially designed loss function ( $\mathcal{L}_F$ ) to supervise the reconstruction of the high-frequency components. In this way, we can enable the network to focus more on the high-frequency components during the reconstruction process, thus achieving better preservation and reconstruction of the high-frequency components.

Based on experimental results, it can be observed that  $\mathbb{R}$  integrated with discrete wavelet transform performs better in SPET reconstruction than U-Net. Specifically, as depicted

in Figure 5, the SPET images predicted by Methods II and III exhibit more distinct boundaries, compared to Method I, particularly in the unclear tissue regions, as highlighted by red bounding boxes in the first row. Additionally, the improvement is evidenced by superior quantitative metrics from Methods II and III that outperform the metrics from Method I, as shown in Table 2. Specifically, Methods II and III exhibit an improvement of 0.498/1.601 dB, 0.002/0.005, and 0.324/0.379 in PSNR, SSIM, and rRMSE, respectively. This serves as further evidence of the effectiveness for the discrete wavelet transform in improving SPET reconstruction.

**Denosing for Sinogram:** In TriPLET, the mapping from LPET to SPET is formulated as both denoising and intensity distribution predictions. By cascading a specialized denoising network  $\mathbb{D}$  to denoise the LPET sinogram before feeding it into the reconstruction network  $\mathbb{R}$ , we can reduce the burden of the reconstruction network and effectively prevent the propagation and amplification of noise in the



subsequent processing, thus achieving better performance in SPET reconstruction.

The effectiveness of denoising for sinograms is demonstrated in the experimental results as presented in Table 2 and Figure 5. Specifically, as shown in Figure 5, both  $\mathbb{D} + \mathbb{R}$  methods (Methods IV and V), which perform denoising first and then reconstruction, achieve better results than the only  $\mathbb{R}$  methods (i.e., Methods II and III). Notably, the SPET images ((e) and (f)) reconstructed using  $\mathbb{D} + \mathbb{R}$  methods have less noise than those ((c) and (d)) by the only  $\mathbb{R}$  methods. In addition, Table 2 shows that  $\mathbb{D} + \mathbb{R}$  methods achieve better performance than the only  $\mathbb{R}$  methods in terms of not only PSNR, but also SSIM, and rRMSE. This verifies that an initial denoising (in the projection domain) step with advanced methods is helpful to boost the reconstruction results, and the cascaded framework of our TriPLET is effective.

**Usefulness of Frequency Loss:** In the reconstruction network  $\mathbb{R}$ , the discrete wavelet transform decomposes the PET image into a series of frequency spectrum maps with different sub-bands. To ensure proper reconstruction of information in each sub-band, we design a specific constraint  $\mathcal{L}_F$  in the wavelet domain for the frequency spectrum maps outputted from  $\mathbb{R}$ .

Comparing the Methods III and II, or Methods V and IV,  $\mathbb{R}$  or  $\mathbb{D} + \mathbb{R}$  can achieve better reconstruction results with the use of additional supervision  $\mathcal{L}_F$  designed in the wavelet domain. Specifically, based on visual results in the second and third rows of Figure 5, it can be observed that the results ((c) and (e)) obtained without  $\mathcal{L}_F$  exhibit artifacts in certain regions, as highlighted by red boxes. In contrast, the results ((d) and (f)) obtained with the inclusion of  $\mathcal{L}_F$  are artifact-free, indicating that the direct supervision of the frequency spectrum map in the wavelet domain effectively prevents errors from propagating to the image domain. As a result, the final prediction image, which incorporates information from all sub-bands, is visually better with overall improved quality. Additionally, quantitative results in Table 2 show that the former methods achieve boosted values of PSNR, SSIM, and rRMSE. These findings suggest that adopting the constraint  $\mathcal{L}_F$  from the wavelet domain can enhance the performance of our WT-based reconstructed network.

Finally,  $\mathbb{D} + \mathbb{R}$  with supervision in all three domains (Method V achieves the best results (i.e., with the lightest color difference maps in Figure 5 and the best PSNR, SSIM, and rRMSE values in Table 2). This proves that all of our proposed loss functions and network components contribute to the final performance.

#### 4.4. Comparison Experiment

We further conducted a comprehensive comparison between our proposed TriPLET and several state-of-the-art SPET enhancement methods, including cGAN (Wang et al., 2018), LA-GAN (Wang et al., 2019), Sinogram-Net (Feng and Liu, 2020), Transformer-GAN (Luo et al., 2021), AR-GAN (Luo et al., 2022), and TriDoRNet (Jiang et al., 2023).

Specifically, cGAN, LA-GAN, Transformer-GAN, and AR-GAN are the GAN-based methods that estimate SPET images from LPET images, while Sinogram-Net and TriDoRNet are a coupled network that directly reconstructs SPET images from LPET sinograms. The quantitative and qualitative results are provided in Table 3 and Figure 6, respectively.

**Quantitative Comparison:** Table 3 presents the quantitative results obtained by different methods, measured in terms of PSNR, SSIM, and rRMSE. Our proposed approach demonstrates superior performance in all aspects. Specifically, when compared to cGAN, which yields the poorest results, our approach achieves significant improvements. We observe an increase of 2.549 dB in PSNR, a 0.010 increase in SSIM, and a reduction of 1.689 in rRMSE. Additionally, our method achieves better performance than TriDoRNet, proving that our improvements based on TriDoRNet are effective. Furthermore, statistical analysis using paired t-tests confirms that the performance of our TriPLET method is significantly better than the optimal performance achieved by other methods. This significance is indicated by the obtained  $p$ -value ( $<0.05$ ) for all evaluation metrics.

These findings provide strong evidence of the effectiveness and superiority of our proposed TriPLET approach in enhancing SPET images, as it outperforms other state-of-the-art methods in terms of both objective measures (PSNR, SSIM, rRMSE) and statistical significance.

**Qualitative Comparison:** The visual results of the comparison methods are presented in Figure 6. It is evident that our approach excels in generating SPET images with several notable characteristics. Firstly, our method achieves the best performance as it can reconstruct SPET images that are closest to the GT, evidenced by having the lightest colored difference maps. Additionally, our method produces SPET images with the clearest boundaries and exhibits superior performance in areas that are difficult to reconstruct (e.g., the bronchial areas shown in the 5th row of Figure 6). In the difference maps, the corresponding boundaries and bronchial areas of our method have the lightest colors. Moreover, our approach effectively minimizes noise, resulting in cleaner images that enhance the visibility of important biological details.

Collectively, these visual comparisons provide substantial evidence supporting the superiority of our approach over state-of-the-art methods. Our method consistently produces SPET images with clear boundaries, reduced noise, enhanced details, and minimal differences from the ground truth, further affirming its superior performance in SPET image generation.

## 5. DISCUSSION

### 5.1. External Validation

Further, we explore the performance of our approach across different PET datasets through external validation. Specifically, we source data from the Ultra Low Dose PET Imaging Challenge Dataset<sup>1</sup>, which is a public dataset that

<sup>1</sup><https://ultra-low-dose-pet.grand-challenge.org/Dataset/>

**Table 4**

Quantitative comparison of external validation, measured by PSNR, SSIM, and rRMSE. The symbol \* indicates the significant difference between the performance of our approach and the optimal performance among other methods, at  $p$ -value  $< 0.05$  level.

Method	PSNR [dB]↑	SSIM ↑	rRMSE ↓
cGAN	22.882 ± 1.753	0.980 ± 0.014	0.782 ± 0.653
LA-GAN	23.123 ± 1.832	0.982 ± 0.013	0.723 ± 0.554
Sinogram-Net	23.132 ± 1.852	0.983 ± 0.011	0.663 ± 0.521
Trans-GAN	23.631 ± 1.635	0.984 ± 0.009	0.496 ± 0.475
AR-GAN	24.524 ± 0.972	0.985 ± 0.008	0.397 ± 0.462
TriDoRNet	24.643 ± 0.913	0.987 ± 0.006	0.348 ± 0.315
TriPLET (ours)	<b>25.146 ± 0.862*</b>	<b>0.989 ± 0.005*</b>	<b>0.312 ± 0.256*</b>

includes paired SPET and corresponding LPET data acquired from Siemens Biograph Vision Quadra and United Imaging uEXPLORER scanners. From this dataset, we collect 40 pairs of SPET and their corresponding 1/10th LPET data as the external validation set. During external validation, all methods are trained on the internal dataset and then directly tested on the external validation set, with the corresponding SPET reconstruction results presented in Table 4. The results indicate that, even on the external validation dataset, our TriPLET outperforms other SPET reconstruction methods, further validating the effectiveness of our TriPLET. Moreover, our TriPLET shows the smallest performance difference between the external validation dataset and the internal dataset, indicating that compared to other methods, our TriPLET possesses the best robustness across various PET datasets.

## 5.2. Curse of Dimensionality

The curse of dimensionality (E. Samadi, Kiefer, Fritsch, Bickenbach and Schuppert, 2022) is a common challenge in data analysis, machine learning, and statistics. It describes the phenomenon where the amount of data samples required for analyzing data or training models grows exponentially with the increase in dimensions. The curse of dimensionality also exists in three-dimensional medical image analysis tasks, including ours. Three-dimensional medical images typically consist of a vast number of voxels, with each voxel representing a feature dimension. This results in extremely high data dimensions, and each dimension may hold important medical information, complicating tasks such as image generation and reconstruction.

In our work, we adopt several strategies to combat the curse of dimensionality. These include: 1) Regularization. We utilize Dropout techniques during the training process to randomly omit (i.e., set to zero) a portion of the neurons in the network. This approach can be considered a model averaging technique that helps mitigate the risk of overfitting and enhances the model's ability to generalize; 2) Data dimensionality reduction. Our framework incorporates an encoder-decoder structure (i.e., sub-network  $\mathbb{R}$ ). Through the encoder, we can effectively reduce the dimensionality of the input data while preserving essential information; 3) The

multi-stage training strategy, where we divide the training of TriPLET into three stages. In this way, we can significantly reduce the number of network parameters that need to be trained in each stage, thus reducing the reliance on training data and computational resources; 4) Data augmentation and five-fold cross-validation. During the data preprocessing stage, we extract 40 overlapping patches from each whole PET image, increasing the number of data samples from 70 to 2800. This not only expands our dataset but also reduces the network input size, thereby lessening the dependence on GPU memory. Moreover, the use of five-fold cross-validation during training allows us to make more efficient use of the augmented data.

## 5.3. The Impact of Data Diversity and Quality

The quality and diversity of data significantly impact tasks involving the reconstruction and generation of medical images. Factors such as noise, outliers, and a lack of data diversity can lead to poor model training outcomes, which in turn can affect the accuracy and reliability of the generated or reconstructed images.

In our work, we have employed a series of strategies to mitigate the impacts of these factors. Firstly, during the data preprocessing phase, we filter each PET image's values (i.e., only retaining values within the 5% to 95% range) to eliminate outliers, thereby removing their influence on subsequent tasks. We then normalize the range of all image values to [0,1] through z-score normalization to further eliminate the interference of noise and outliers. Secondly, by extracting 40 overlapping patches from each whole PET image, we increase the data samples from 70 to 2800. This method significantly enhances data diversity, enabling the trained model to possess stronger generalization. Lastly, in the model design phase, based on the principles of PET imaging, we decompose the task of mapping from LPET to SPET into two simpler tasks (namely, denoising and reconstruction tasks). In this way, we can more stably and robustly predict SPET from LPET, and the preliminary denoising network can further reduce the impact of noise on our task. Through the above strategies, we effectively minimize the impact of data quality and diversity on our task. Using the same data to train models, our proposed TriPLET



achieves superior SPET reconstruction results compared to other methods, with the results provided in Table 3 and Figure 6.

## 6. CONCLUSION

In this work, we develop a novel end-to-end TriPle-domain LPET EnhancemT (TriPLET) framework for reconstructing SPET Images from LPET sinograms, by considering a hybrid denoising-and-reconstruction process and simultaneously taking the advantages of projection, wavelet, and image domains into the enhancement procedure. Specifically, TriPLET couples three networks to sequentially perform sinogram denoising in the projection domain, SPET reconstruction in the wavelet domain, and image evaluation in the image domain. Furthermore, we specifically design three loss functions respective to the three domains for supervising the training of TriPLET. Through experiments conducted on real human chest-abdomen PET data, we demonstrate that TriPLET is designed effectively and can also achieve the best quantitative and qualitative results than state-of-the-art methods.

## Declaration of Competing Interest

The authors declare that they have no known competing financial interests or personal relationships that could have appeared to influence the work reported in this paper.

## CRedit Authorship Contribution Statement

**Caiwen Jiang:** Conceptualization, Methodology, Software, Writing - original draft, Validation. **Mianxin Liu:** Investigation, Conceptualization, Writing - review & editing. **Kaicong Sun:** Investigation, Supervision, Writing - review & editing. **Dinggong Shen:** Conceptualization, Supervision, Project administration, Writing - review & editing, Funding acquisition.

## Ethical and Data Availability Statement

This work involved human subjects or animals in its research. Approval of all ethical and experimental procedures and protocols was granted by the Institute Research Medical Ethics Committee of Zhongshan Hospital, Fudan University.

## Acknowledgments

This work was supported in part by the National Natural Science Foundation of China under Grant 62131015 and 82394432, the Science and Technology Commission of Shanghai Municipality (STCSM) under Grant 21010502600, and the Key Research and Development Program of Guangdong Province, China, under Grant 2021B0101420006.

## References

Abouhawwash, M., Alessio, A., 2022. Evolutionary optimization of multiple machine-learned objectives for PET image reconstruction. *IEEE Transactions on Radiation and Plasma Medical Sciences* 7, 273–283.

- Amirrahedi, M., Sarkar, S., Ghadiri, H., Ghafarian, P., Ay, M., 2021. Standard-dose PET reconstruction from low-dose preclinical images using an adopted all convolutional U-Net. *Biomedical Applications in Molecular, Structural, and Functional Imaging* 11600, 834–848.
- An, L., Zhang, P., Adeli, E., Wang, Y., Ma, G., Shi, F., Lalush, D.S., Lin, W., Shen, D., 2016. Multi-level canonical correlation analysis for standard-dose PET image estimation. *IEEE Transactions on Image Processing* 25, 3303–3315.
- Arabi, H., Zaidi, H., 2018. Improvement of image quality in PET using post-reconstruction hybrid spatial-frequency domain filtering. *Physics in Medicine & Biology* 63, 215010.
- Avril, N.E., Weber, W.A., 2005. Monitoring response to treatment in patients utilizing PET. *Radiologic Clinics* 43, 189–204.
- Ba, J.L., Kiros, J.R., Hinton, G.E., 2016. Layer normalization. *arXiv preprint arXiv:1607.06450*.
- Bailey, D.L., Maisey, M.N., Townsend, D.W., Valk, P.E., 2006. Positron Emission Tomography : Basic sciences. *Journal of Neuroradiology* 33, 265–265.
- Barbosa, F., Queiroz, M.A., Nunes, R.F., Costa, L.B., Zaniboni, E.C., Marin, J.G., Cerri, G.G., Buchpiguel, C.A., 2020. Nonprostatic diseases on PSMA PET imaging: a spectrum of benign and malignant findings. *Cancer Imaging* 20, 1–23.
- Bhavana, V., Krishnappa, H., 2015. Multi-modality medical image fusion using discrete wavelet transform. *Procedia Computer Science* 70, 625–631.
- Breiman, L., 2001. Random forests. *Machine Learning* 45, 5–32.
- Brunet, D., Vrscay, E., Wang, Z., 2011. On the mathematical properties of the structural similarity index. *IEEE Transactions on Image Processing* 21, 1488–1499.
- Buades, A., Coll, B., Morel, J., 2005. A non-local algorithm for image denoising. *2005 IEEE computer society conference on Computer Vision and Pattern Recognition* 2, 60–65.
- Buchbender, C., Heusner, T.A., Lauenstein, T.C., Bockisch, A., Antoch, G., 2012. Oncologic PET/MRI, part 1: tumors of the brain, head and neck, chest, abdomen, and pelvis. *Journal of Nuclear Medicine* 53, 928–938.
- Byrd, D., Dasari, P., Jansen, F., Kinahan, P., 2023. Impact of subsets and iterations on PET image quality in TOF-OSEM reconstruction , 1–1.
- Carion, N., Massa, F., Synnaeve, G., Usunier, N., Kirillov, A., Zagoruyko, S., 2020. End-to-end object detection with transformers. *European Conference on Computer Vision* , 213–229.
- Chan, C., Meikle, S., Fulton, R., Tian, G., Cai, W., Feng, D., 2009. A non-local post-filtering algorithm for PET incorporating anatomical knowledge. *2009 IEEE Nuclear Science Symposium Conference Record* , 2728–2732.
- Chen, W., 2007a. Clinical applications of PET in brain tumors. *Journal of Nuclear Medicine* 48, 1468–1481.
- Chen, W., 2007b. Clinical applications of PET in brain tumors. *Journal of Nuclear Medicine* 48, 1468–1481.
- Chen, Z., Badrinarayanan, V., Lee, C., Rabinovich, A., 2018. GradNorm: Gradient normalization for adaptive loss balancing in deep multitask networks. *International Conference on Machine Learning* , 794–803.
- Cho, S., Chun, S.Y., Reese, T., Fakhri, G., Zhu, X., Ouyang, J., Catana, C., Guerin, B., 2010. Compensation for nonrigid motion using B-spline image registration in simultaneous MR-PET. *International Society for Magnetic Resonance in Medicine* .
- Çiçek, Ö., Abdulkadir, A., Lienkamp, S., Brox, T., Ronneberger, O., 2016. 3D U-Net: Learning dense volumetric segmentation from sparse annotation. *International Conference on Medical Image Computing and Computer-Assisted Intervention* , 424–432.
- Cui, J., Gong, K., Guo, N., Wu, C., Meng, X., Kim, K., Zheng, K., Wu, Z., Fu, L., Xu, B., et al., 2019. PET image denoising using unsupervised deep learning. *European journal of nuclear medicine and molecular imaging* 46, 2780–2789.
- Dabov, K., Foi, A., Katkovnik, V., Egiazarian, K., 2006. Image denoising with block-matching and 3D filtering 6064, 354–365.
- Daerr, S., Brendel, M., Zach, C., Mille, E., Rominger, A., 2016. Evaluation of early-phase [18F]-florbetaben PET acquisition in clinical routine cases. *Neuroimage Clinical* 14.

- Daubechies, I., 1990. The wavelet transform, time-frequency localization and signal analysis. *IEEE transactions on information theory* 36, 961–1005.
- Daubechies, I., 2009. The wavelet transform, time-frequency localization and signal analysis .
- Decazes, P., Hinault, P., Veresezan, O., Thureau, S., Gouel, P., Vera, P., 2021. Trimodality PET/CT/MRI and radiotherapy: A mini-review. *Frontiers in Oncology* 10, 3392.
- Diaz-Pinto, A., Colomer, A., Morales, S., Xu, Y., Frangi, A., 2019. Retinal image synthesis and semi-supervised learning for glaucoma assessment. *IEEE Transactions on Medical Imaging* 38, 2211–2218.
- Dimitrakopoulou-Strauss, A., Pan, L., Sachpekidis, C., 2021. Kinetic modeling and parametric imaging with dynamic PET for oncological applications: General considerations, current clinical applications, and future perspectives. *European Journal of Nuclear Medicine and Molecular Imaging* 48, 21–39.
- Dutta, J., Leahy, R., Li, Q., 2013. Non-local means denoising of dynamic PET images. *PLoS One* 8, e81390.
- E. Samadi, M., Kiefer, S., Fritsch, S.J., Bickenbach, J., Schuppert, A., 2022. A training strategy for hybrid models to break the curse of dimensionality. *Plos One* 17, e0274569.
- Fahey, F., 2002. Data acquisition in PET imaging. *Journal of Nuclear Medicine Technology* 30, 39–49.
- Feng, E., Qin, P., Chai, R., Zeng, J., Wang, Q., Meng, Y., Wang, P., 2022. MRI generated from CT for acute ischemic stroke combining radiomics and generative adversarial networks. *IEEE Journal of Biomedical and Health Informatics* .
- Feng, Q., Liu, H., 2020. Rethinking PET image reconstruction: Ultra-low-dose, sinogram and deep learning. *International Conference on Medical Image Computing and Computer-Assisted Intervention* , 783–792.
- Fortunato, S., 2010. Community detection in graphs. *Phys. Rep.-Rev. Sec. Phys. Lett.* 486, 75–174.
- Geng, P., Tan, Z., Wang, Y., Jia, W., Zhang, Y., Yan, H., 2024. STCNet: Alternating CNN and improved transformer network for COVID-19 CT image segmentation. *Biomedical Signal Processing and Control* 93, 106205.
- Gigengack, F., Ruthotto, L., Burger, M., Wolters, C.H., Jiang, X., Schafers, K.P., 2012. Motion correction in dual gated cardiac PET using mass-preserving image registration. *IEEE Transactions on Medical Imaging* 31, 698–712.
- Goodfellow, I., Pouget-Abadie, J., Mirza, M., Xu, B., Warde-Farley, D., Ozair, S., Courville, A., Bengio, Y., 2014. Generative adversarial nets. *Advances in Neural Information Processing Systems* 27, 100–109.
- Gu, J., Yang, T., Ye, J., Yang, D., 2021. CycleGAN denoising of extreme low-dose cardiac CT using wavelet-assisted noise disentanglement. *Medical Image Analysis* 74, 102209.
- Hägström, I., Schmidlein, C., Campanella, G., Fuchs, T., 2019. DeepPET: A deep encoder–decoder network for directly solving the PET image reconstruction inverse problem. *Medical Image Analysis* 54, 253–262.
- Hamill, J., Michel, C., Kinahan, P., 2003. Fast PET EM reconstruction from linograms. *IEEE Transactions on Nuclear Science* 50, 1630–1635.
- Händel, P., 2018. Understanding normalized mean squared error in power amplifier linearization. *IEEE Microwave and Wireless Components Letters* 28, 1047–1049.
- Hofheinz, F., Langner, J., Beuthien-Baumann, B., Oehme, L., Steinbach, J., Kotzerke, J., Hoff, J., 2011. Suitability of bilateral filtering for edge-preserving noise reduction in PET. *EJNMMI Research* 1, 1–9.
- Hong, Q., Lin, L., Li, Z., Li, Q., Yao, J., Wu, Q., Liu, K., Tian, J., 2023. A distance transformation deep forest framework with hybrid-feature fusion for CRX image classification. *IEEE Transactions on Neural Networks and Learning Systems* .
- Hu, C., Zhang, Y., Zhang, W., Liao, P., Wang, G., 2017. Low-dose CT via convolutional neural network. *Biomedical Optics Express* 8, 679.
- Hu, S., Yu, W., Chen, Z., Wang, S., 2020. Medical image reconstruction using generative adversarial network for alzheimer disease assessment with class-imbalance problem. *2020 IEEE 6th International Conference on Computer and Communications (ICCC)* , 1323–1327.
- Huang, J., Guan, L., Chen, Y., Zhu, S., Chen, L., Yu, J., 2022. A deep learning scheme for transient stability assessment in power system with a hierarchical dynamic graph pooling method. *International Journal of Electrical Power & Energy Systems* 141, 108044.
- Hullermeier, E., Rifqi, M., 2009. A fuzzy variant of the rand index for comparing clustering structures. in: in *Proc. IFSA/EUSFLAT Conf.*, pp. 1294–1298.
- Ioffe, S., Szegedy, C., 2015. Batch normalization: Accelerating deep network training by reducing internal covariate shift. *International Conference on Machine Learning* , 448–456.
- Isola, P., Zhu, J., Zhou, T., Efros, A., 2017. Image-to-image translation with conditional adversarial networks. *Proceedings of the IEEE conference on computer vision and pattern recognition* , 1125–1134.
- Jia, H., Wu, G., Wang, Q., Shen, D., 2010. ABSORB: Atlas building by self-organized registration and bundling. *NeuroImage* 51, 1057–1070.
- Jia, H., Yap, P., Shen, D., 2012. Iterative multi-atlas-based multi-image segmentation with tree-based registration. *NeuroImage* 59, 422–430.
- Jiang, C., Pan, Y., Cui, Z., Shen, D., 2022. Reconstruction of standard-dose PET from low-dose PET via dual-frequency supervision and global aggregation module. *2022 IEEE 19th International Symposium on Biomedical Imaging (ISBI)* , 1–5.
- Jiang, C., Pan, Y., Shen, D., 2023. Tridornet: Reconstruction of standard-dose PET from low-dose PET in triple (projection, image, and frequency) domains , 1–5.
- Jiang, L., Dai, B., Wu, W., Loy, C.C., 2021. Focal frequency loss for image reconstruction and synthesis. *Proceedings of the IEEE/CVF International Conference on Computer Vision* , 13919–13929.
- Kamnitsas, K., Ledig, C., Newcombe, V., Simpson, J.P., Kane, A.D., Menon, D.K., Rueckert, D., Glocker, B., 2016. Efficient multi-scale 3D CNN with fully connected CRF for accurate brain lesion segmentation. *Medical Image Analysis* 36, 61.
- Kamran, S., Hossain, K., Tavakkoli, A., Zuckerbrod, S., Baker, S., 2021. ViGAN: Semi-supervised retinal image synthesis and disease prediction using vision transformers. *Proceedings of the IEEE/CVF International Conference on Computer Vision* , 3235–3245.
- Kang, J., Gao, Y., Shi, F., Lalush, D.S., Lin, W., Shen, D., 2015. Prediction of standard-dose brain PET image by using MRI and low-dose brain [18F]FDG PET images. *Medical Physics* 42, 5301–5309.
- Katsevich, A., 2004. An improved exact filtered backprojection algorithm for spiral computed tomography. *Advances in Applied Mathematics* 32, 681–697.
- Kawahara, J., Brown, C.J., Miller, S.P., Booth, B.G., Hamarneh, G., 2017. BrainNetCNN: Convolutional neural networks for brain networks; towards predicting neurodevelopment. *NeuroImage* 146, 1038–1049.
- Kim, K., Wu, D., Gong, K., Dutta, J., Kim, J., Son, Y., Kim, H., F., E., Li, Q., 2018. Penalized PET reconstruction using deep learning prior and local linear fitting. *IEEE Transactions on Medical Imaging* 37, 1478–1487.
- Kleesiek, J., Urban, G., Hubert, A., Schwarz, D., Maier-Hein, K., Bendszus, M., Biller, A., 2016. Deep MRI brain extraction: A 3D convolutional neural network for skull stripping. *NeuroImage* 129, 460–469.
- Korhonen, J., You, J., 2012. Peak signal-to-noise ratio revisited: Is simple beautiful? *2012 Fourth International Workshop on Quality of Multimedia Experience* , 37–38.
- Kreisl, W.C., Kim, M., Coughlin, J.M., Henter, I.D., Owen, D.R., Innis, R.B., 2020. PET imaging of neuroinflammation in neurological disorders. *The Lancet Neurology* 19, 940–950.
- Lehtinen, J., Munkberg, J., Hasselgren, J., Laine, S., Karras, T., Aittala, M., Aila, T., 2018. Noise2Noise: Learning image restoration without clean data. *arXiv preprint arXiv:1803.04189* .
- Lei, Y., Dong, X., Wang, T., Higgins, K., Yang, X., 2020. Estimating standard-dose PET from low-dose PET with deep learning. *Image Processing* 113, 73–82.
- Li, Y., Cui, J., Chen, J., Zeng, G., Wollenweber, S., Jansen, F., Jang, S., Kim, K., Gong, K., Li, Q., 2022. A noise-level-aware framework for PET image denoising. *arXiv preprint arXiv:2203.08034* .
- Li, Y., Zhang, K., Shi, W., Miao, Y., Jiang, Z., 2021. A novel medical image denoising method based on conditional generative adversarial network. *Computational and Mathematical Methods in Medicine* 2021, 1–11.

- Li, Z., Huang, J., Yu, L., Chi, Y., Jin, M., 2019. Low-dose CT image denoising using cycle-consistent adversarial networks. 2019 IEEE Nuclear Science Symposium and Medical Imaging Conference (NSS/MIC), 1–3.
- Liang, J., Yang, X., Huang, Y., Li, H., He, S., Hu, X., Chen, Z., Xue, W., Cheng, J., Ni, D., 2022. Sketch guided and progressive growing GAN for realistic and editable ultrasound image synthesis. *Medical Image Analysis* 79, 102461.
- Liaw, A., Wiener, M., 2002. Classification and regression by randomforest. *R News* 2, 18–22.
- Liu, P., Zhang, H., Zhang, K., Lin, L., Zuo, W., 2018. Multi-level wavelet-CNN for image restoration. *Proceedings of the IEEE conference on computer vision and pattern recognition workshops*, 773–782.
- Liu, Z., Lin, Y., Cao, Y., Hu, H., Wei, Y., Zhang, Z., Lin, S., Guo, B., 2021. Swin transformer: Hierarchical vision transformer using shifted windows. *Proceedings of the IEEE/CVF International Conference on Computer Vision*, 10012–10022.
- Lu, W., Onofrey, J., Lu, Y., Shi, L., Ma, T., Liu, Y., Liu, C., 2019. An investigation of quantitative accuracy for deep learning based denoising in oncological PET. *Physics in Medicine & Biology* 64, 165019.
- Lu, Z., Li, Z., Wang, J., Shen, D., 2021. Two-stage self-supervised cycle-consistency network for reconstruction of thin-slice MR images. *arXiv preprint arXiv:2106.15395*.
- Luo, Y., Wang, Y., Zu, C., Zhan, B., Wu, X., Zhou, J., Shen, D., Zhou, L., 2021. 3D transformer-GAN for high-quality PET reconstruction. *International Conference on Medical Image Computing and Computer-Assisted Intervention*, 276–285.
- Luo, Y., Zhou, L., Zhan, B., Fei, Y., Zhou, J., Wang, Y., Shen, D., 2022. Adaptive rectification based adversarial network with spectrum constraint for high-quality PET image synthesis. *Medical Image Analysis* 77, 102335.
- Maurer, L., Wang, J., 2005. Positron Emission Tomography: applications in drug discovery and drug development. *Current Topics in Medicinal Chemistry* 5, 1053–1075.
- Mehranian, A., Reader, A., 2020. Model-based deep learning PET image reconstruction using forward-backward splitting expectation-maximization. *IEEE Transactions on Radiation and Plasma Medical Sciences* 5, 54–64.
- Meyer, J.H., Cervenka, S., Kim, M., Kreis, W.C., Henter, I.D., Innis, R.B., 2020. Neuroinflammation in psychiatric disorders: PET imaging and promising new targets. *The Lancet Psychiatry*.
- Mokri, S., Saripan, M., R., A., Nordin, A., Hashim, S., Marhaban, M., 2016. PET image reconstruction incorporating 3D mean-median sinogram filtering. *IEEE Transactions on Nuclear Science* 63, 157–169.
- Mosconi, L., Tsui, W.H., Herholz, K., Pupi, A., Drzezga, A., Lucignani, G., Reiman, E.M., Holthoff, V., Kalbe, E., Sorbi, S., 2008. Multicenter standardized 18F-FDG PET diagnosis of mild cognitive impairment, Alzheimer's disease, and other dementias. *Journal of Nuclear Medicine* 49, 390–398.
- Newman, M.E.J., 2013. Network data. <http://www-personal.umich.edu/~mejn/netdata/>.
- Nguyen, H., Bai, L., 2010. Cosine similarity metric learning for face verification. *Asian Conference on Computer Vision*, 709–720.
- Nguyen, V., Lee, S., 2013. Incorporating anatomical side information into PET reconstruction using nonlocal regularization. *IEEE Transactions on Image Processing* 22, 3961–3973.
- Nichols, T., Qi, J., Asma, E., Leahy, R., 2002. Spatiotemporal reconstruction of list-mode pet data. *IEEE Transactions on Medical Imaging* 21, 396–404.
- Olesen, O.V., Sullivan, J.M., Mulnix, T., Paulsen, R.R., Hojgaard, L., Roed, B., Carson, R.E., Morris, E.D., Larsen, R., 2013. List-mode PET motion correction using markerless head tracking: Proof-of-concept with scans of human subject. *IEEE Transactions on Medical Imaging* 32, 200–209.
- Onishi, Y., Hashimoto, F., Ote, K., Ohba, H., Ota, R., Yoshikawa, E., Ouchi, Y., 2021. Anatomical-guided attention enhances unsupervised PET image denoising performance. *Medical Image Analysis* 74, 102226.
- Ote, K., Hashimoto, F., Kakimoto, A., Isobe, T., Inubushi, T., Ota, R., Tokui, A., Saito, A., Moriya, T., Omura, T., 2020. Kinetics-induced block matching and 5-D transform domain filtering for dynamic PET image denoising. *IEEE Transactions on Radiation and Plasma Medical Sciences* 4, 720–728.
- P., L., Hanzouli, H., Hatt, M., R., L., Visvikis, D., 2013. Denoising of PET images by combining wavelets and curvelets for improved preservation of resolution and quantitation. *Medical Image Analysis* 17, 877–891.
- Pan, Y., Liu, M., Lian, C., Xia, Y., Shen, D., 2020. Spatially-constrained fisher representation for brain disease identification with incomplete multi-modal neuroimages. *IEEE Transactions on Medical Imaging* 39, 2965–2975.
- Pan, Y., Liu, M., Xia, Y., Shen, D., 2021. Disease-image-specific learning for diagnosis-oriented neuroimage synthesis with incomplete multi-modality data. *IEEE Transactions on Pattern Analysis and Machine Intelligence* 27, 1675–1686.
- Park, T., Liu, M., Wang, T., Zhu, J., 2019. Semantic image synthesis with spatially-adaptive normalization. *Proceedings of the IEEE/CVF Conference on Computer Vision and Pattern Recognition*, 2337–2346.
- Peiris, H., Hayat, M., Chen, Z., Egan, G., Harandi, M., 2022. A robust volumetric transformer for accurate 3D tumor segmentation. *International Conference on Medical Image Computing and Computer-Assisted Intervention*, 162–172.
- Ronneberger, O., Fischer, P., Brox, T., 2015. U-net: Convolutional networks for biomedical image segmentation. *International Conference on Medical image computing and computer-assisted intervention*, 234–241.
- Sakthivel, P., Thakar, A., Prashanth, A., Angamuthu, M., Sharma, S.C., Kumar, R., 2020. Clinical applications of 68 ga-psma PET/CT on residual disease assessment of juvenile nasopharyngeal angiofibroma (JNA). *Nuclear Medicine and Molecular Imaging* 54, 63–64.
- Schaefferkoetter, J., Yan, J., Ortega, C., Sertic, A., Lechtman, E., Eshet, Y., Metser, U., Veit-Haibach, P., 2020. Convolutional neural networks for improving image quality with noisy pet data. *EJNMMI research* 10, 1–11.
- Shukla, P.D., 2003. Complex wavelet transforms and their applications. A Dissertation Submitted of Signal Processing Division, Department of Electronic and Electrical Engineering University of Strathclyde Scotland United Kingdom.
- Slovis, Thomas, L., 2002. The ALARA concept in pediatric CT: myth or reality? *Radiology* 223, 5–6.
- Song, T., Yang, F., Dutta, J., 2021. Noise2Void: unsupervised denoising of PET images. *Physics in Medicine & Biology* 66, 214002.
- Souza, R., Lebel, R.M., Frayne, R., 2019. A hybrid, dual domain, cascade of convolutional neural networks for magnetic resonance image reconstruction. *International Conference on Medical Imaging with Deep Learning*, 437–446.
- Spencer, B., Berg, E., Schmall, J., Omidvari, N., Leung, E., Abdelhafez, Y.G., Tang, S., Deng, Z., Dong, Y., Lv, Y., 2021. Performance evaluation of the uEXPLORER total-body PET/CT scanner based on NEMA NU 2-2018 with additional tests to characterize pet scanners with a long axial field of view. *Journal of Nuclear Medicine* 62, 861–870.
- Spurr, A., Aksan, E., Hilliges, O., 2017. Guiding infoGAN with semi-supervision. *Joint European Conference on Machine Learning and Knowledge Discovery in Databases*, 119–134.
- Sun, L., Wang, J., Huang, Y., Ding, X., Greenspan, H., Paisley, J., 2020. An adversarial learning approach to medical image synthesis for lesion detection. *IEEE Journal of Biomedical and Health Informatics* 24, 2303–2314.
- Tang, J., Rahmim, A., 2014. Anatomy assisted PET image reconstruction incorporating multi-resolution joint entropy. *Physics in Medicine & Biology* 60, 31.
- Toft, P., 1996. The radon transform. *Theory and Implementation* (Ph. D. Dissertation)(Copenhagen: Technical University of Denmark).
- Ulyanov, D., Vedaldi, A., Lempitsky, V., 2016. Instance normalization: The missing ingredient for fast stylization. *arXiv preprint arXiv:1607.08022*.
- Umehara, K., Ota, J., Ishida, T., 2017. Super-resolution imaging of mammograms based on the super-resolution convolutional neural network. *Open Journal of Medical Imaging* 07, 180–195.
- Wang, Y., Ma, G., An, L., Shi, F., Zhang, P., Wu, X., Zhou, J., Shen, D., 2016. Semi-supervised triple dictionary learning for standard-dose

- PET image prediction using low-dose PET and multimodal MRI. *IEEE Transactions on Biomedical Engineering* 64, 569–579.
- Wang, Y., Yu, B., Wang, L., Zu, C., Lalush, D.S., Lin, W., Wu, X., Zhou, J., Shen, D., Zhou, L., 2018. 3D conditional generative adversarial networks for high-quality PET image estimation at low dose. *Neuroimage* 174, 550–562.
- Wang, Y., Zhang, P., An, L., Ma, G., Kang, J., Shi, F., Wu, X., Zhou, J., Lalush, D.S., Lin, W., 2015. Predicting standard-dose PET image from low-dose PET and multimodal MR images using mapping-based sparse representation. *Physics in Medicine & Biology* 61, 791–801.
- Wang, Y., Zhou, L., Yu, B., Wang, L., Zu, C., Lalush, D.S., Lin, W., Wu, X., Zhou, J., Shen, D., 2019. 3D auto-context-based locality adaptive multi-modality GANs for PET synthesis. *IEEE Transactions on Medical Imaging* 38, 1328–1339.
- Wang, Z., Bovik, A., Sheikh, H., Simoncelli, E., 2004. Image quality assessment: from error visibility to structural similarity. *IEEE Transactions on Image Processing* 13, 600–612.
- Wasserthal, J., Meyer, M., Breit, H., Cyriac, J., Yang, S., Segeroth, M., 2022. Totalsegmentator: robust segmentation of 104 anatomical structures in CT images. *arXiv preprint arXiv:2208.05868*.
- Williams, O., Blake, A., Cipolla, R., 2005. Sparse Bayesian learning for efficient visual tracking. *IEEE Transactions on Pattern Analysis and Machine Intelligence* 27, 1292–1304.
- Willmott, C., Matsuura, K., 2005. Advantages of the mean absolute error (MAE) over the root mean square error (RMSE) in assessing average model performance. *Climate Research* 30, 79–82.
- Wu, G., Jia, H., Wang, Q., Shen, D., 2011. SharpMean: groupwise registration guided by sharp mean image and tree-based registration. *NeuroImage* 56, 1968–1981.
- Wu, W., Hu, D., Niu, C., Yu, H., Vardhanabhuti, V., Wang, G., 2021. DRONE: Dual-domain residual-based optimization network for sparse-view CT reconstruction. *IEEE Transactions on Medical Imaging*.
- Wu, Y., He, K., 2018. Group normalization. *Proceedings of the European Conference on Computer Vision (ECCV)*, 3–19.
- Xiang, L., Qiao, Y., Nie, D., An, L., Lin, W., Wang, Q., Shen, D., 2017. Deep auto-context convolutional neural networks for standard-dose PET image estimation from low-dose PET/MRI. *Neurocomputing* 267, 406–416.
- Xiang, L., Wang, L., Gong, E., Zaharchuk, G., Zhang, T., 2020. Noise-aware standard-dose PET reconstruction using general and adaptive robust loss. *International Workshop on Machine Learning in Medical Imaging*, 654–662.
- Xiao, J., Yu, L., Xing, L., Yuille, A., Zhou, Y., 2021. DualNorm-UNet: Incorporating global and local statistics for robust medical image segmentation. *arXiv preprint arXiv:2103.15858*.
- Xu, J., Gong, E., Pauly, J., Zaharchuk, G., 2017. 200x low-dose PET reconstruction using deep learning. *arXiv preprint arXiv:1712.04119*.
- Xuan, K., Si, L., Zhang, L., Xue, Z., Wang, Q., 2020. Reduce slice spacing of MR images by super-resolution learned without ground-truth. *arXiv preprint arXiv:2003.12627*.
- Yan, J., Lim, J., Townsend, D., 2015. MRI-guided brain PET image filtering and partial volume correction. *Physics in Medicine & Biology* 60, 961.
- Yang, D., He, X., Zhang, R., 2023. Alternating attention Transformer for single image deraining. *Digital Signal Processing*, 104144.
- Yang, H., Sun, J., Carass, A., Zhao, C., Lee, J., Prince, J., Xu, Z., 2020. Unsupervised MR-to-CT synthesis using structure-constrained cycleGAN. *IEEE Transactions on Medical Imaging* 39, 4249–4261.
- Yi, X., Walia, E., Babyn, P., 2019. Generative adversarial network in medical imaging: A review. *Medical image analysis* 58, 101552.
- Yie, S., Kang, S., Hwang, D., Lee, J., 2020. Self-supervised PET denoising. *Nuclear Medicine and Molecular Imaging* 54, 299–304.
- Yurt, M., Dar, S., Erdem, A., Erdem, E., Oguz, K., Çukur, T., 2021. mustGAN: multi-stream generative adversarial networks for MR image synthesis. *Medical Image Analysis* 70, 101–144.
- Zeng, L.L., Gao, K., Hu, D., Feng, Z., Hou, C., Rong, P., Wang, W., 2023. SS-TBN: a semi-supervised tri-branch network for COVID-19 screening and lesion segmentation. *IEEE Transactions on Pattern Analysis and Machine Intelligence*.
- Zhang, K., Zuo, W., Chen, Y., Meng, D., Zhang, L., 2017. Beyond a gaussian denoiser: Residual learning of deep CNN for image denoising. *IEEE Transactions on Image Processing* 26, 3142–3155.
- Zhang, X., Xie, Z., Berg, E., Judenhofer, M.S., Liu, W., Xu, T., Ding, Y., Lv, Y., Dong, Y., Deng, Z., 2020. Total-body dynamic reconstruction and parametric imaging on the uEXPLORER. *Journal of Nuclear Medicine* 61, 285–291.
- Zhou, B., Chen, X., Zhou, S., Duncan, J., Liu, C., 2022. DuDoDR-Net: Dual-domain data consistent recurrent network for simultaneous sparse view and metal artifact reduction in computed tomography. *Medical Image Analysis* 75, 102289.
- Zhou, L., Schaefferkoetter, J., Tham, I., Huang, G., Yan, J., 2020. Supervised learning with CycleGAN for low-dose FDG PET image denoising. *Medical Image Analysis* 65, 101770.
- Zhu, J.Y., Park, T., Isola, P., Efros, A.A., 2017. Unpaired image-to-image translation using cycle-consistent adversarial networks. *Proceedings of the IEEE International Conference on Computer Vision*, 2223–2232.